

# Coating Porous MXene Films with Tunable Porosity for High-Performance Solid-State Supercapacitors

Sina Abdolhosseinzadeh,<sup>[a, b]</sup> Jakob Heier,<sup>[a]</sup> and Chuanfang (John) Zhang<sup>\*[a]</sup>

Two-dimensional MXenes with their outstanding physical and chemical properties have been extensively used in numerous fields such as electrochemical energy storage, catalysis, and sensing. In these applications, high active surface area and facilitated diffusion of ions/atoms/molecules are crucial. While these features can be offered by porous films and structures, their fabrication at ambient conditions, especially with scalable methods such as printing and coating has proven to be quite challenging. Here, we have developed MXene inks containing a

space-holder agent, based on which porous films with tunable porosities can be easily coated. The whole fabrication process lasts only a few minutes and is carried out at room temperature and pressure, making it suitable for continuous scalable production. Films with different porosities (up to 80 %) have been coated and used for the fabrication of solid-state micro-supercapacitors with enhanced rate capability and improved capacitance (241 mF/cm<sup>2</sup>).

## 1. Introduction

Two-dimensional transition metal carbides and nitrides (MXenes), with their excellent electrical properties, abundant functional groups and rich surface chemistry,<sup>[1]</sup> have shown great promise in numerous applications such as electrochemical energy storage,<sup>[2]</sup> catalysis,<sup>[3]</sup> sensing,<sup>[4]</sup> etc. MXenes have a general formula of  $M_{n+1}X_nT_x$ , where M is an early transition metal (Ti, V, Nb, Cr, Ta, Mo, etc.), X is carbon and/or nitrogen, and  $T_x$  represents surface terminal groups (–O, –OH, –F, –Cl, –Br, etc.).<sup>[1,5–8]</sup> MXenes are typically obtained by etching out the A element (group 13 or 14, such as Al, Si, Ga, etc.) from the parent MAX phase either by HF-based etching methods,<sup>[9–12]</sup> hydrothermal treatment in concentrated basic solutions,<sup>[13]</sup> or halide molten salts strategies.<sup>[14,15]</sup>

Owing to their unique physicochemical properties, MXenes can be readily dispersed in various solvents and processed into coatable/printable inks, which can form robust films after deposition (and drying).<sup>[16]</sup> Nevertheless, processing of conventional MXene colloidal suspensions result in films/coatings with a densely packed morphology. This inevitably reduces the accessible surface area and obstructs the ion diffusion


pathways,<sup>[17]</sup> leading to a compromised performance for the aforementioned applications.<sup>[18]</sup> Since the electrical properties of MXene films or structures depend on their packing density (inter-flake junctions),<sup>[19]</sup> optimizing the porosity of the films is necessary for maximizing their performance, and in particular their electrochemical charge storage properties.


Amongst various methods for production of porous MXene films and structures, freeze-drying is arguably the most widely used technique.<sup>[20–22]</sup> Nevertheless, the required long processing time, low pressure, and low temperature, limit its practicality. Other techniques such as supercritical drying,<sup>[5]</sup> hydrazine treatment,<sup>[23]</sup> and sacrificial-template<sup>[24]</sup> methods also suffer from non-ambient processing conditions (e.g. high pressure, high temperature) and/or involve hazardous chemical reactions. Although some low- or room-temperature methods based on coating MXenes on non-sacrificial templates<sup>[25]</sup> or forming Pickering emulsions<sup>[26]</sup> are reported, controlling the size of the pores or porosity levels are still challenging. Very recently, Tang et al. reported a facile method based on oxidation with sulfuric acid to create favorable ion diffusion pathways in MXene freestanding films, however, the usage of concentrated sulfuric acid pose extra potential risk during the synthesis of materials.<sup>[27]</sup> Hence, for cost-effective production of porous MXene films and their potential applications in energy storage devices, novel, industrially-scalable techniques with low (no) environmental/safety concerns should be developed.

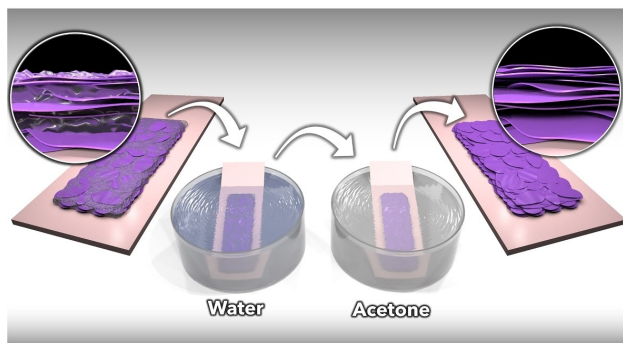
Here we report an efficient and straightforward method for coating (and printing) porous MXene films with tunable porosity. Such a route is based on the addition of a space-holder (such as urea)<sup>[28]</sup> to the MXene ink and removing it after deposition and drying of the film (Scheme 1). The porosity level is easily adjustable, and no toxic chemicals or solvents are involved (see Experimental Section). More importantly, the whole process is carried out at ambient conditions and lasts only a few minutes. We demonstrate that the porous MXene films showcase excellent charge storage properties when used as solid-state micro-supercapacitor (MSC) electrodes, including

[a] S. Abdolhosseinzadeh, Dr. J. Heier, Dr. C. (J.) Zhang  
Laboratory for Functional Polymers  
Swiss Federal Laboratories for Materials Science and Technology (Empa)  
Überlandstrasse 129, CH-8600 Dübendorf, Switzerland  
E-mail: chuanfang.zhang@empa.ch

[b] S. Abdolhosseinzadeh  
Institute of Materials Science and Engineering  
Ecole Polytechnique Fédérale de Lausanne (EPFL)  
Station 12, CH-1015 Lausanne, Switzerland

 An invited contribution to a joint Special Collection between ChemElectroChem and Batteries & Supercaps dedicated to research Beyond Lithium-Ion Batteries

 © 2021 The Authors. ChemElectroChem published by Wiley-VCH GmbH. This is an open access article under the terms of the Creative Commons Attribution Non-Commercial NoDerivs License, which permits use and distribution in any medium, provided the original work is properly cited, the use is non-commercial and no modifications or adaptations are made.



**Scheme 1.** Three main steps of fabrication of porous MXene films with the space-holder technique. First (from left), MXene inks containing a space-holder (urea) is coated on a substrate. After drying, the space-holder is leached out of the film in water. While porosities are still filled with water, the film is merged in a low boiling point solvent (acetone) to replace the water. Finally, by fast evaporation of the acetone (e.g. by hot air stream), a porous MXene film is obtained.

high areal capacitance and long-term lifespan. It is worth noting that the proposed strategy in creating porosity in films/coatings should also be effective for other 2D materials beyond MXenes, ensuring improved device-level performance at much reduced costs.

## 2. Results and Discussions

We start by describing the as-synthesized  $\text{Ti}_3\text{C}_2\text{T}_x$  MXene, which was obtained by etching the  $\text{Ti}_3\text{AlC}_2$  MAX phase (Figure 1a) via a minimally intensive layer delamination (MILD) route<sup>[29]</sup> (see Experimental Section). The obtained product, which is multi-layer MXene (Figure 1b), was delaminated to single/few layered MXene by vigorous vortex mixing to obtain large and high-quality flakes (Figure 1c). Transmission electron microscopy (TEM) verifies the complete delamination process and presence

of few-layer MXene flakes with large lateral size (Figure 1d). This is further confirmed by X-ray diffraction (XRD). As shown in figure 2a, the characteristic peaks of  $\text{Ti}_3\text{AlC}_2$  MAX phase have disappeared and a strong peak at about  $7.3^\circ$  has evolved, which is attributed to the (002) plane of  $\text{Ti}_3\text{C}_2\text{T}_x$  MXene.<sup>[30]</sup>

After the delamination process, delaminated MXene flakes were transferred to an organic solvent (*N*-methyl-2-pyrrolidone, NMP) to improve the wettability of the ink and adhesion of the film (see Experimental Section). It should be noted that when wetting and adhesion of the aqueous inks to the substrate is acceptable (e.g. paper), transferring to organic solvents is not necessary. High solid content inks ( $\sim 8$  wt.%) were formulated to deposit thick films in each coating pass (Figure 2b). At such high concentrations, MXenes form colloidal gels (Figure 2c) with very high viscosities. However, since inks exhibit significant shear-thinning behavior, which follows the Ostwald-de Waele model ( $\eta = K\dot{\gamma}^{n-1}$ ; Figure 2d), the viscosity drops down to much lower values at high shear rates, making them suitable for processing by various coating techniques (e.g. blade coating). From the double logarithmic plot of viscosity vs. shear rate (Figure 2d inset) and fitting a line to its linear region, the power-law index which is a measure of the pseudoplasticity of the ink<sup>[31]</sup> was calculated to be  $\sim 0.1$ . Both porous and compact films showcase almost identical Raman spectra (Figure 2e) with all the expected vibrational modes of  $\text{Ti}_3\text{C}_2\text{T}_x$ .<sup>[32]</sup> No other peak

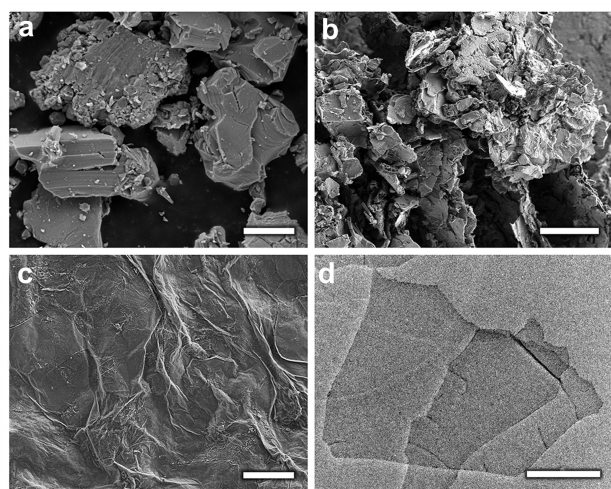


**Figure 1.** SEM images of a) MAX phase (scale bar: 4  $\mu\text{m}$ ), b) multi-layer MXene (scale bar: 10  $\mu\text{m}$ ), and c) delaminated MXene (scale bar: 3  $\mu\text{m}$ ). d) TEM image of the large flake delaminated MXene (scale bar: 1  $\mu\text{m}$ ).

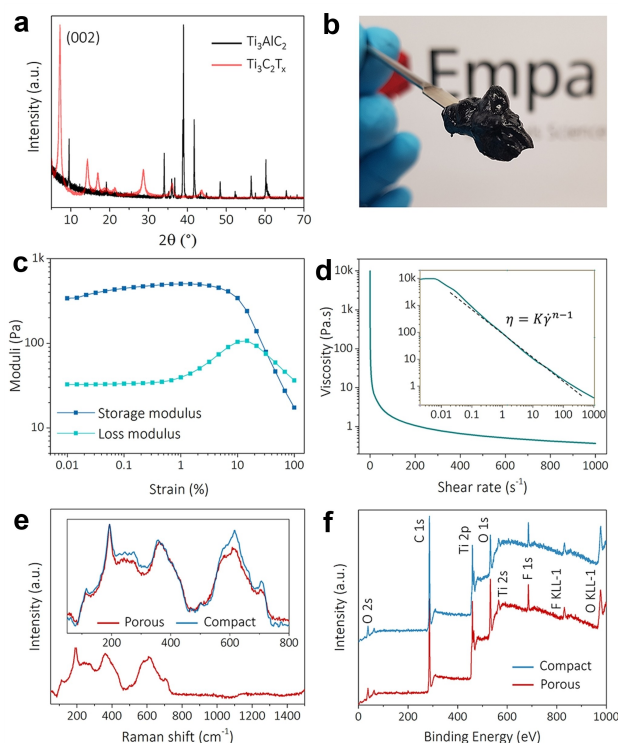


**Figure 2.** a) XRD patterns of  $\text{Ti}_3\text{AlC}_2$  MAX phase and delaminated  $\text{Ti}_3\text{C}_2\text{T}_x$  MXene. b) Digital photograph of a MXene ink with 5 wt.% urea. c) The rheological characterization (amplitude sweep test) of the ink shown in (b). d) Flow curves of the ink shown in (b). Inset is the same graph plotted in a log-log scale to show the power-law behavior of the ink and calculate the power-law index. e) Raman and f) XPS spectra of porous and compact (pristine) films coated on a PET substrate.

(e.g. anatase<sup>[33]</sup> or urea)<sup>[34]</sup> is observable, suggesting that the urea has been fully removed and no compositional change (e.g. oxidation) has occurred during this process. This is further confirmed by the X-ray photoelectron spectroscopy (XPS) where no nitrogen peak is detectable in the survey spectrum of the porous film (Figure 2f).

The porosity level of the films can be easily adjusted by varying the concentration of the added space-holder (Figure 3a–d). The density of the pristine MXene films (lowest porosity) were found to be  $\sim 2.11 \text{ g/cm}^3$ , which is lower than the vacuum filtered films.<sup>[35,36]</sup> Low compaction level of the films is a general issue in printed/coated particle based inks.<sup>[37]</sup> The lowest achievable density was  $1.15 \text{ g/cm}^3$ , which corresponds to  $\sim 80\%$  porosity (considering the theoretical density of the  $-\text{OH}$  terminated  $\text{Ti}_3\text{C}_2$ :  $5.2 \text{ g/cm}^3$ ).<sup>[10]</sup> Pristine MXene films typically feature smooth surfaces with a metallic sheen (Figure 3e). By addition of urea, the films lose their metallic sheen and turn black. In this stage, since porosities are still filled with urea, a feature-less, flat and relatively smooth surface is observed in SEM images (Figure 3f). Once the urea is leached out of the film, the black color turns gray and the porous structure (with a rough surface) becomes visible in the SEM images (Figure 3g). After dissolving out the space holder and upon evaporation of

the residual solvents, the porosity may slightly decrease due to the capillary forces formed within the pores. The porosities can be preserved by exchanging the residual solvent (used for dissolving the space holder) with a low boiling point solvent (Figure 3h).  $\text{N}_2$  adsorption/desorption Brunauer-Emmett-Teller (BET) tests were conducted to study the pore characteristics of the samples. The specific surface area increases significantly from  $10.5 \text{ m}^2/\text{g}$  (for films coated with the urea-free ink) to  $95.6 \text{ m}^2/\text{g}$  (coated with highest urea content ink). The hysteresis loops in type IV physisorption isotherms (Figure 3i) suggest a mesoporous structure<sup>[38]</sup> with pore sizes mainly ranging from 10–70 nm (Figure 3i-inset).

The straightforward and adjustable fabrication of porous films/structures can potentially impact a broad range of applications including lightweight foams, gas sorption, removal of hazardous metal ions, electromagnetic interference shielding, energy storage, etc., where a high porosity is preferred. As such, we choose MSCs as a model to evaluate the electrochemical charge storage performance of the coated porous films and demonstrate some of their potential applications. MSCs are of particular interest since  $\text{Ti}_3\text{C}_2\text{T}_x$  MXene possesses a metal oxide-like surface and metallic conductivity, allowing fast surface redox reactions proceeding in a pseudocapacitive behavior,<sup>[39,40]</sup>

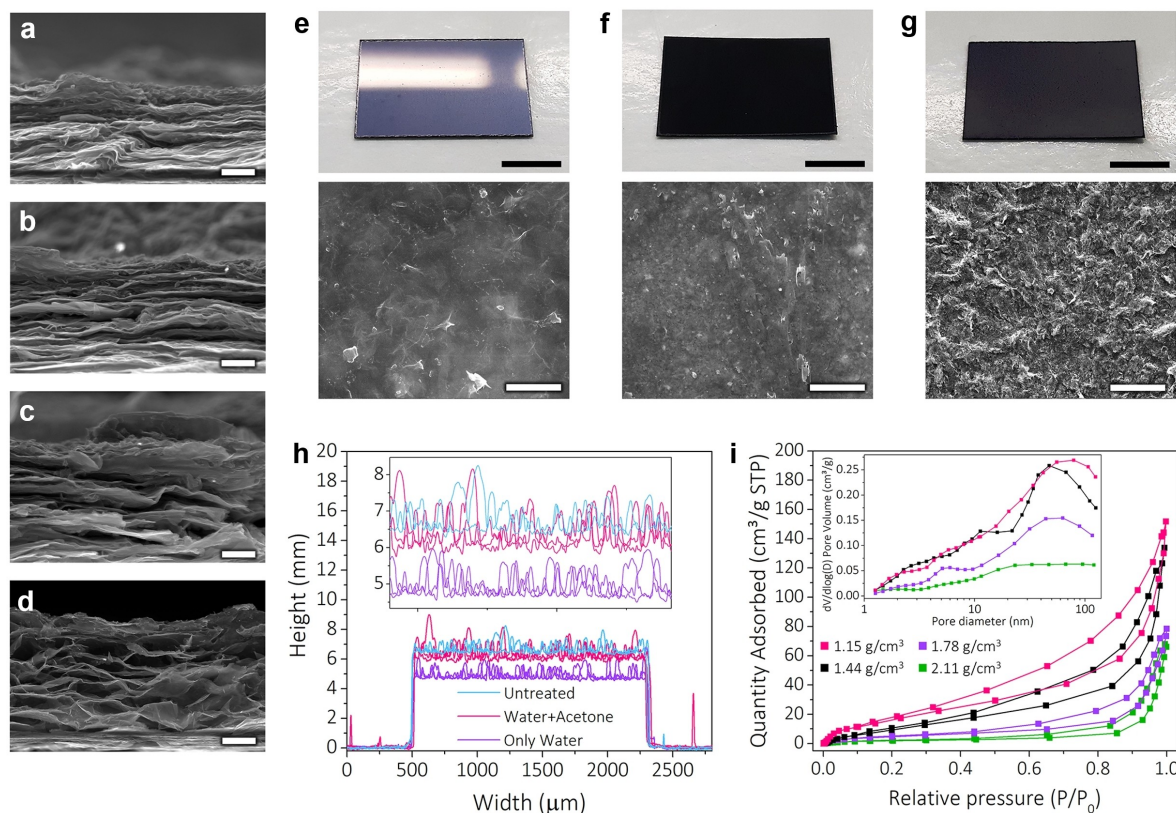


**Figure 3.** SEM images of the films with different densities. a) Pristine film,  $2.11 \text{ g/cm}^3$ ; b)  $1.78 \text{ g/cm}^3$ ; c)  $1.44 \text{ g/cm}^3$ ; d)  $1.15 \text{ g/cm}^3$ . The scale bar in all figures (a–d), including the close-up image of (d), is  $2 \mu\text{m}$ . Digital photographs (top, all scale bar:  $2 \text{ cm}$ ) and SEM images (bottom, all scale bars:  $30 \mu\text{m}$ ) of e) pristine MXene film; f) MXene film with urea; and g) porous MXene film after the removal of the urea. h) Height profiles of two different porous films (laser-scribed), treated (urea dissolution) only with water and “water and acetone”. The height profile of the film before treatment is also shown for reference. Every height profile was measured three times by a mechanical profilometer. i) BET  $\text{N}_2$  adsorption/desorption analysis of the films coated with different urea content inks (specific surface areas:  $95.6 \text{ m}^2/\text{gr}$  ( $1.15 \text{ g/cm}^3$ ),  $62.1 \text{ m}^2/\text{gr}$  ( $1.44 \text{ g/cm}^3$ ),  $24.3 \text{ m}^2/\text{gr}$  ( $1.78 \text{ g/cm}^3$ ),  $10.5 \text{ m}^2/\text{gr}$  ( $2.11 \text{ g/cm}^3$ )).



both in supercapacitors and aqueous metal-ion (such as Na, Zn, etc.) batteries.<sup>[24,41–43]</sup>

To fabricate the MSCs, several inks with different urea but similar MXene contents were formulated (see Experimental Section) and blade coated on a polyethylene terephthalate (PET) substrate. The thickness of the wet films was adjusted to deposit similar amounts of MXene to ensure a fair comparison. After removing the urea and drying the films at room-temperature, interdigitated electrodes (1 cm<sup>2</sup> footprint area, ~120  $\mu$ m gap size) were made by laser scribing (Figure 4a). Due to their high conductivity, MXene films also act as a current collector. The fabrication of the MSCs was accomplished by addition of a sulfuric acid (H<sub>2</sub>SO<sub>4</sub>)-poly vinyl alcohol (PVA) gel electrolyte.<sup>[19]</sup>

Cyclic voltammetry (CV) tests were carried out on devices with 4 different porosity levels (Figure 4b). Increasing the scan rate inevitably results in reduced capacitance (Figure 4c); however, porous films exhibit better capacity retention than their pristine counterparts (62% vs. 39% when increasing the scan rate from 5 mV/s to 200 mV/s). In addition to the rate capability, the specific capacitance of the devices also signifi-

cantly depends on the porosity level of the films. As shown in figure 4d, by increasing the porosity, the specific capacitance increases from 153 F/g (193 mF/cm<sup>2</sup>) to a maximum value of 192 F/g (241 mF/cm<sup>2</sup>) for films with the density of 1.44 g/cm<sup>3</sup> and then severely drops down to 110 F/g (138 mF/cm<sup>2</sup>, film density of 1.15 g/cm<sup>3</sup>). The increase in the capacitance can be well explained by the enhanced accessibility of ions to sites where pseudocapacitive redox reactions can take place. On the other hand, the drop in the capacitance at higher porosity levels can be attributed to the interrupted conducting network of the particles and larger inter-flake resistance (Figure 4e).

To further investigate these observations, we performed electrochemical impedance spectroscopy (EIS) tests. The Nyquist plots (Figure 4f) reveal that all the samples have almost similar series resistance ( $R_s$ , the highest porosity has a slightly higher resistance), which is the sum of the contact resistance and the electrolyte resistance (the intercepts on the X-axis at high frequency region). However, by increasing the porosity, the curve becomes more vertical in the low frequency region, indicative of the improved capacitive behavior and facilitated

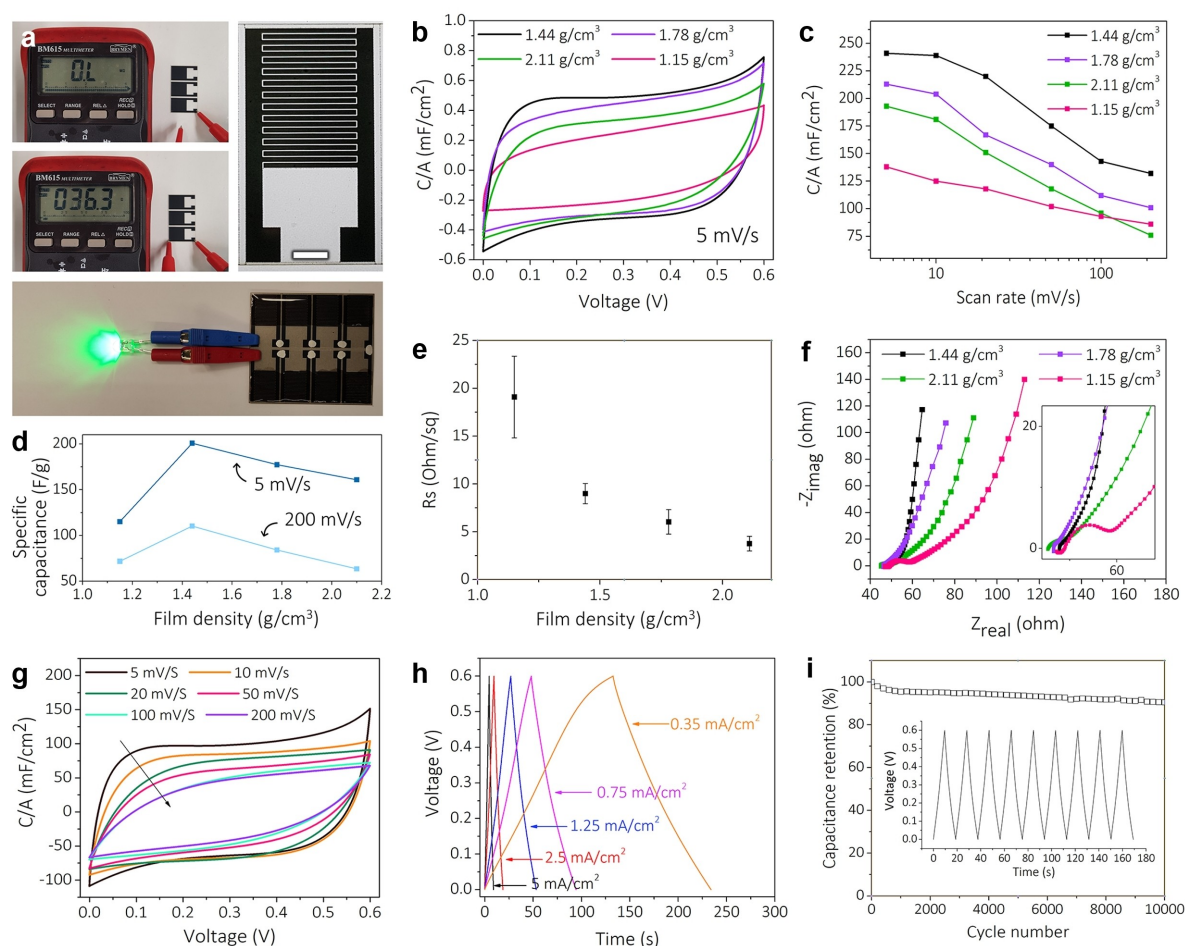


**Figure 4.** a) Digital photographs of laser-scribed interdigitated MSC electrodes (scale bar: 3 mm), and a tandem device powering an LED. b) CV profiles of MSCs made of films with different densities at a scan rate of 5 mV/s. c) Areal capacitances of the devices described in (b) at different scan rate. d) Gravimetric capacitance at different film densities. e) Sheet-resistance of the films with different densities (note that all films have similar amounts of MXene). f) Electrochemical impedance spectroscopy of the MSCs with different film densities. g) Normalized CV profiles of a MSC with a film density of 1.44 g/cm<sup>3</sup>. h) Galvanostatic-charge-discharge results of the devices described in (g). i) Long-term cycling of the device described in (g).

ion diffusion pathways. Further increasing the porosity leads to a substantial increase in the internal charge-transfer resistance ( $R_{ct}$ , the semicircle part).

The CV and EIS tests results suggest that the highest capacitance and the best rate capability are only achieved when the porosity of the films has been optimized (in this work 72%). Since the electrical conductivity of the films has a profound effect on the device performance, it is expected that MXenes with different synthesis routes and/or physicochemical properties (e.g. flake size, density of the functional groups) will exhibit different optimum porosity levels. The mechanical properties of the porous films also heavily depend on the physicochemical properties. Our efforts in making porous films with small flake multilayer MXene on glass substrate (see Experimental Section) were not successful mainly due to the inferior cohesion of the flakes and adhesion of the films to the substrate. In other words, the morphological and intrinsic properties of MXenes mainly govern the cohesion/adhesion of the resultant films/coatings, and certainly deserve to be studied further in the future.

In acidic electrolytes, protons interact with the hydroxyl groups of MXene (terminal groups) leading to the continuous valence change of the transition metal (here Ti). As a result, MXene exhibits a perfect pseudocapacitive behavior,<sup>[40]</sup> which can be seen in the rectangular-shaped CV and symmetric linear galvanostatic-charge-discharge (GCD) plots (Figure 4g, h). This ideal capacitive behavior was also previously verified by the Nyquist plots with the almost vertical curves in the low frequency region (Figure 4f). Areal capacitances derived from CV and GCD curves have comparable values and maximum areal capacitance of 241 mF/cm<sup>2</sup> and energy density of 3  $\mu$ Wh/cm<sup>2</sup> were obtained for the MSCs with the optimum porosity (72%). This device also showcases an excellent cycling performance, retaining 90.5% of the initial capacitance after 10000 cycles without parasitic reactions involved (Figure 4i and inset). Furthermore, as compared in Table 1, this device outperforms most other MSCs with similar materials and comparable fabrication methods in terms of areal capacitance and energy density.

### 3. Conclusions

In summary, we have reported a novel method for the production of porous MXene films/structures with controllable porosity for high-performance electrochemical energy storage devices. This method can also be used for other applications such as catalysis and sensing where the active surface area and/or ion-diffusion kinetics matter. While we have discussed the formulation of blade-coating inks, by changing the concentration of MXene and adjusting the rheological properties, inks for other printing and coating methods can be easily formulated as well. We have found that the porosity level should be optimized for every application/material since higher porosities are associated with the degradation of other properties (e.g. electrical, mechanical). We have demonstrated the application of our method for the fabrication of highly rate capable, high capacitance microsupercapacitors. Considering that the energy storage devices are commercially produced in enormously large scales, extremely fast electrode fabrication processes are needed. Therefore, our method can be a promising candidate for industrial production of porous electrodes for high-performance electrochemical energy storage devices.

### Experimental Section

#### Etching of the MAX phase

A minimally intensive layer delamination or "MILD" synthesis route was used for etching the Al layer from Ti<sub>3</sub>AlC<sub>2</sub> MAX phase. Typically, first, 0.5 g of lithium fluoride (LiF, Sigma Aldrich, USA) was gradually dissolved in 10 mL of 9 M hydrochloric acid (HCl, 37 wt.%, Sigma Aldrich, USA), maintaining the temperature close to room temperature. Once the LiF is fully dissolved in HCl, 0.5 g of Ti<sub>3</sub>AlC<sub>2</sub> MAX phase (average particle size ~38  $\mu$ m, YCarbon, Ukraine) was slowly added to the above mixture under vigorous stirring. The reaction continued for 24 h at room temperature at a stirring speed of 300 rpm. Finally (after 24 h), the etched MAX phase was separated from the etching solution by centrifuging it at 1500 rcf for 3 min (relative centrifugal force). To purify the etched MAX phase, the supernatant was decanted, and 40 mL of fresh DI water was added and vigorously shook for 1 min. The supernatant was again separated by centrifugation at 3500 rcf for 3 min. After repeating the washing process for 5 times (pH of the supernatant reached ~6), purified etched MAX phase was collected from the sediments of the last centrifugation process.

**Table 1.** Specific energy density and areal capacitance comparison of various MSCs.

Material	Fabrication method	Specific capacitance per electrode [mF/cm <sup>2</sup> ]	Specific energy density [ $\mu$ Wh/cm <sup>2</sup> ]	Ref.
Ti <sub>3</sub> C <sub>2</sub> T <sub>x</sub>	Screen printing	158 (0.08 mA/cm <sup>2</sup> )	1.64	[2]
Ti <sub>3</sub> C <sub>2</sub> T <sub>x</sub> @RuO <sub>2</sub>	Screen printing	23.3 (1 mV/s)	0.36	[44]
Ti <sub>3</sub> C <sub>2</sub> T <sub>x</sub> /CoAl	Screen printing	40 (0.75 mA/cm <sup>2</sup> )	10.8	[45]
Ti <sub>3</sub> C <sub>2</sub> T <sub>x</sub>	Extrusion printing	43 (5 $\mu$ A/cm <sup>2</sup> )	0.32	[7]
Ti <sub>3</sub> C <sub>2</sub> T <sub>x</sub>	Spray coating + Laser scribing	27.3 (20 mV/s)	2.34	[46]
Ti <sub>3</sub> C <sub>2</sub> T <sub>x</sub>	Spray coating + Laser scribing	23 (0.1 mA/cm <sup>2</sup> )	1.12	[47]
Ti <sub>3</sub> C <sub>2</sub> T <sub>x</sub> /RGO	Spray coating (with mask)	2.4 (2 mV/s)	0.26	[48]
Ti <sub>3</sub> C <sub>2</sub> T <sub>x</sub>	Spray coating (with mask)	3.26 (5 mV/s)	0.34	[49]
Ti <sub>3</sub> C <sub>2</sub> T <sub>x</sub>	Blade coating + Laser cutting	52 (2 mA/cm <sup>2</sup> )	2.62	[50]
Ti <sub>3</sub> C <sub>2</sub> T <sub>x</sub>	Meyer rod coating + Laser scribing	25 (20 mV/s)	0.77	[51]
Ti <sub>3</sub> C <sub>2</sub> T <sub>x</sub>	Blade coating + Laser scribing	241 (5 mV/s)	3	This work

## Delamination of the MXene

The obtained MAX phase majorly consists of multi-layer MXene and unetched (or partially etched) MAX phase. Two different routes were used for the delamination of the multi-layer MXene into single or few layers, resulting in two products with different flake sizes. Large flakes were obtained by vigorous vortex mixing (VORTEXER-Heathrow) at 3000 rpm and small flakes were obtained via ultrasonic treatment (in a bath sonicator) under the protective stream of Ar gas for 15 mins. Finally, to separate the delaminated nanosheets from the multi-layered MXene and un-etched MAX, another centrifugation step at 1500 rcf for 30 min is needed.

## Ink formulation

The obtained delaminated MXene suspension has a low concentration and is not suitable for blade coating. To increase the solid content, we centrifuged the suspension at 15000 rcf for 1 h. The obtained sediments were added to 40 ml *N*-Methyl-2-pyrrolidone (NMP) and shook vigorously in a vortex mixer for 10 mins. The obtained suspension was then centrifuged at 15000 rcf for another 1 h. This process was repeated once more to fully transfer the MXene to NMP. Four identical inks with 8 wt.% MXene in NMP were prepared and to three of them urea was added with the following concentrations: 3.5 wt.%, 4.5 wt.%, and 6.5 wt.%. For adding the urea, it was first dissolved in water with the concentration of 36.5 wt.%.

## Coating porous films

Inks with different urea content were blade coated on PET substrates. After complete drying, films were immersed in DI water for 5 mins. This process was repeated two more times in a fresh DI water. Afterwards, films (while having water inside the pores) were transferred to an acetone bath for 1 min and then dried by hot air stream.

## Gel electrolyte preparation

Typically, 1 g of polyvinyl alcohol (PVA) powder was added to 10 ml of DI-water. Then the mixture was stirred vigorously at 85 °C until the solution became clear. After cooling down, 3 g of concentrated H<sub>2</sub>SO<sub>4</sub> (97 wt.%) was dropwise added and mixed with the above solution, followed by another 1 h of vigorous stirring at room temperature.

## Electrochemical characterization

The charge storage performance of the fabricated MSCs was evaluated through CV and GCD on a VMP3 potentiostat (BioLogic, France). The devices were tested at different CV scan rates (from 5 to 200 mV/s) and GCD current densities (from 0.35 to 5 mA/cm<sup>2</sup>) in a voltage window of 0.6 V. Electrochemical impedance spectroscopy was performed at open-circuit voltage from 100 mHz to 100 kHz. The areal capacitance per electrode was calculated from the stabilized (fifth) CV curve according to the following equation [Eq. (1)]:

$$\frac{C}{A} = \frac{4}{A_t \Delta V \nu} \int_0^{0.6} j dV \quad (1)$$

Where,  $C/A$  is the measured areal capacitance (mF/cm<sup>2</sup>),  $j$  is the current (mA),  $\Delta V$  is the voltage window (0.6 V),  $A_t$  (cm<sup>2</sup>) is the geometric area of the MSC,  $\nu$  is the scan rate (mV/s).

In the devices that showcased symmetric, linear GCD curves, the areal capacitance was also obtained from the stabilized (fifth) GCD curves according to the following equation [Eq. (2)]:

$$\frac{C}{A} = \frac{4j \Delta t}{A_t \Delta V} \quad (2)$$

Where  $\Delta V$  is the effective voltage window after the  $IR$  drop,  $\Delta t$  is the discharge time.

## Acknowledgments

Financial supports from the project FOXIP in the framework of the Strategic Focus Area (SFA) Advanced Manufacturing of the ETH Board and internal research grants (IRC 2019 and IRC 2020) of Empa are acknowledged.

## Conflict of Interest

The authors declare no conflict of interest.

**Keywords:** MXene • supercapacitor • coating • porous film • foam

- [1] B. Anasori, M. R. Lukatskaya, Y. Gogotsi, *Nat. Rev. Mater.* **2017**, 2, 16098.
- [2] S. Abdolhosseinzadeh, R. Schneider, A. Verma, J. Heier, F. Nüesch, C. Zhang, *Adv. Mater.* **2020**, 32, 2000716.
- [3] D. Zhao, Z. Chen, W. Yang, S. Liu, X. Zhang, Y. Yu, W. C. Cheong, L. Zheng, F. Ren, G. Ying, X. Cao, D. Wang, Q. Peng, G. Wang, C. Chen, *J. Am. Chem. Soc.* **2019**, 141, 4086–4093.
- [4] S. J. Kim, H. J. Koh, C. E. Ren, O. Kwon, K. Maleski, S. Y. Cho, B. Anasori, C. K. Kim, Y. K. Choi, J. Kim, Y. Gogotsi, H. T. Jung, *ACS Nano* **2018**, 12, 986–993.
- [5] Y. Xia, T. S. Mathis, M.-Q. Zhao, B. Anasori, A. Dang, Z. Zhou, H. Cho, Y. Gogotsi, S. Yang, *Nature* **2018**, 557, 409–412.
- [6] M. Naguib, V. N. Mochalin, M. W. Barsoum, Y. Gogotsi, *Adv. Mater.* **2014**, 26, 992–1005.
- [7] C. (John) Zhang, L. McKeon, M. P. Kremer, S. H. Park, O. Ronan, A. Seral-Ascaso, S. Barwich, C. Coileáin, N. McEvoy, H. C. Nerl, B. Anasori, J. N. Coleman, Y. Gogotsi, V. Nicolosi, *Nat. Commun.* **2019**, 10, 1795.
- [8] C. (John) Zhang, S. H. Park, A. Seral-Ascaso, S. Barwich, N. McEvoy, C. S. Boland, J. N. Coleman, Y. Gogotsi, V. Nicolosi, *Nat. Commun.* **2019**, 10, 849.
- [9] M. Naguib, M. Kurtoglu, V. Presser, J. Lu, J. Niu, M. Heon, L. Hultman, Y. Gogotsi, M. W. Barsoum, *Adv. Mater.* **2011**, 23, 4248–53.
- [10] M. Naguib, O. Mashtalir, J. Carle, V. Presser, J. Lu, L. Hultman, Y. Gogotsi, M. W. Barsoum, *ACS Nano* **2012**, 6, 1322–31.
- [11] A. Lipatov, M. Alhabeab, M. R. Lukatskaya, A. Boson, Y. Gogotsi, A. Sinitskii, *Adv. Electron. Mater.* **2016**, 2, 1600255.
- [12] F. Du, H. Tang, L. Pan, T. Zhang, H. Lu, J. Xiong, J. Yang, C. (John) Zhang, *Electrochim. Acta* **2017**, 235, 690–699.
- [13] T. Li, L. Yao, Q. Liu, J. Gu, R. Luo, J. Li, X. Yan, W. Wang, P. Liu, B. Chen, W. Zhang, W. Abbas, R. Naz, D. Zhang, *Angew. Chem. Int. Ed. Engl.* **2018**, 130, 6223–6227.
- [14] Y. Li, H. Shao, Z. Lin, J. Lu, L. Liu, B. Duployer, P. O. Å. Å. Persson, P. Eklund, L. Hultman, M. Li, K. Chen, X.-H. H. Zha, S. Du, P. Rozier, Z. Chai, E. Raymundo-Piñero, P.-L. L. Taberna, P. Simon, Q. Huang, *Nat. Mater.* **2020**, 19, 894–899.
- [15] V. Kamysbayev, A. S. Filatov, H. Hu, X. Rui, F. Lagunas, D. Wang, R. F. Klie, D. V. Talapin, *Science* **2020**, eaba8311.
- [16] S. Abdolhosseinzadeh, J. Heier, C. (John) Zhang, *J. Phys. Energy* **2020**, 2, 31004.

- [17] G. Tontini, M. Greaves, S. Ghosh, V. Bayram, S. Barg, *J. Phys. Mater.* **2020**, 3, 22001.
- [18] S. J. Kim, M. Naguib, M. Zhao, C. Zhang, H.-T. Jung, M. W. Barsoum, Y. Gogotsi, *Electrochim. Acta* **2015**, 163, 246–251.
- [19] C. J. Zhang, B. Anasori, A. Seral-Ascaso, S.-H. Park, N. McEvoy, A. Shmeliov, G. S. Duesberg, J. N. Coleman, Y. Gogotsi, V. Nicolosi, *Adv. Mater.* **2017**, 29, 1702678.
- [20] S. Zhao, H. B. Zhang, J. Q. Luo, Q. W. Wang, B. Xu, S. Hong, Z. Z. Yu, *ACS Nano* **2018**, 12, 11193–11202.
- [21] W. Yang, J. Yang, J. J. Byun, F. P. Moissinac, J. Xu, S. J. Haigh, M. Domingos, M. A. Bissett, R. A. W. Dryfe, S. Barg, *Adv. Mater.* **2019**, 31, 1902725.
- [22] Z. Zeng, C. Wang, G. Siqueira, D. Han, A. Huch, S. Abdolhosseinzadeh, J. Heier, F. Nüesch, C. (John) Zhang, G. Nyström, *Adv. Sci.* **2020**, 2000979.
- [23] J. Liu, H.-B. Zhang, R. Sun, Y. Liu, Z. Liu, A. Zhou, Z.-Z. Yu, *Adv. Mater.* **2017**, 29, 1702367.
- [24] M.-Q. Zhao, X. Xie, C. E. Ren, T. Makaryan, B. Anasori, G. Wang, Y. Gogotsi, *Adv. Mater.* **2017**, 29, 1702410.
- [25] Y. Yue, N. Liu, W. Liu, M. Li, Y. Ma, C. Luo, S. Wang, J. Rao, X. Hu, J. Su, Z. Zhang, Q. Huang, Y. Gao, *Nano Energy* **2018**, 50, 79–87.
- [26] R. Bian, R. Lin, G. Wang, G. Lu, W. Zhi, S. Xiang, T. Wang, P. S. Clegg, D. Cai, W. Huang, *Nanoscale* **2018**, 10, 3621–3625.
- [27] J. Tang, T. Mathis, X. Zhong, X. Xiao, H. Wang, M. Anayee, F. Pan, B. Xu, Y. Gogotsi, *Adv. Energy Mater.* **2021**, 2003025.
- [28] S. Sadighikia, S. Abdolhosseinzadeh, H. Asgharzadeh, *Powder Metall.* **2015**, 58, 61–66.
- [29] A. Lipatov, M. Alhabeb, M. R. Lukatskaya, A. Boson, Y. Gogotsi, A. Sinitskii, *Adv. Electron. Mater.* **2016**, 2, 1600255.
- [30] M. Alhabeb, K. Maleski, B. Anasori, P. Lelyukh, L. Clark, S. Sin, Y. Gogotsi, *Chem. Mater.* **2017**, 29, 7633–7644.
- [31] S. Abdolhosseinzadeh, X. Jiang, H. Zhang, J. Qiu, C. (John) Zhang, *Mater. Today* **2021**, DOI 10.1016/j.mattod.2021.02.010.
- [32] M. Naguib, M. Kurtoglu, V. Presser, J. Lu, J. Niu, M. Heon, L. Hultman, Y. Gogotsi, M. W. Barsoum, *Adv. Mater.* **2011**, 23, 4248–4253.
- [33] C. J. Zhang, S. Pinilla, N. McEvoy, C. P. Cullen, B. Anasori, E. Long, S.-H. Park, A. Seral-Ascaso, A. Shmeliov, D. Krishnan, C. Morant, X. Liu, G. S. Duesberg, Y. Gogotsi, V. Nicolosi, *Chem. Mater.* **2017**, 29, 4848–4856.
- [34] R. L. Frost, J. Kristof, L. Rintoul, J. T. Klopogge, *Spectrochim. Acta Part A* **2000**, 56, 1681–1691.
- [35] J. Yan, C. E. Ren, K. Maleski, C. B. Hatter, B. Anasori, P. Urbankowski, A. Sarycheva, Y. Gogotsi, *Adv. Funct. Mater.* **2017**, 27, 1701264.
- [36] M. R. Lukatskaya, S. Kota, Z. Lin, M.-Q. Zhao, N. Shpigiel, M. D. Levi, J. Halim, P.-L. Taberna, M. W. Barsoum, P. Simon, Y. Gogotsi, *Nat. Energy* **2017**, 2, 17105.
- [37] A. G. Kelly, T. Hallam, C. Backes, A. Harvey, A. S. Esmaeili, I. Godwin, J. Coelho, V. Nicolosi, J. Lauth, A. Kulkarni, S. Kinge, L. D. A. Siebbeles, G. S. Duesberg, J. N. Coleman, *Science* **2017**, 356, 69–73.
- [38] T. A. Le, N. Q. Tran, Y. Hong, H. Lee, *Chem. Eur. J.* **2019**, 25, 1037–1043.
- [39] C. (John) Zhang, Y. Ma, X. Zhang, S. Abdolhosseinzadeh, H. Sheng, W. Lan, A. Pakdel, J. Heier, F. Nüesch, *Energy Environ. Mater.* **2020**, 3, 29–55.
- [40] M. Hu, Z. Li, T. Hu, S. Zhu, C. Zhang, X. Wang, *ACS Nano* **2016**, 10, 11344–11350.
- [41] X. Li, M. Li, Q. Yang, H. Li, H. Xu, Z. Chai, K. Chen, Z. Liu, Z. Tang, L. Ma, Z. Huang, B. Dong, X. Yin, Q. Huang, C. Zhi, *ACS Nano* **2020**, 14, 541–551.
- [42] N. Zhang, S. Huang, Z. Yuan, J. Zhu, Z. Zhao, Z. Niu, *Angew. Chem. Int. Ed.* **2021**, 60, 2861–2865; *Angew. Chem.* **2021**, 133, 2897–2901.
- [43] C. (John) Zhang, L. Cui, S. Abdolhosseinzadeh, J. Heier, *InfoMat* **2020**, 2, 613–638.
- [44] H. Li, X. Li, J. Liang, Y. Chen, *Adv. Energy Mater.* **2019**, 9, 1803987.
- [45] S. Xu, Y. Dall'Agnese, G. Wei, C. Zhang, Y. Gogotsi, W. Han, *Nano Energy* **2018**, 50, 479–488.
- [46] Y.-Y. Peng, B. Akuzum, N. Kurra, M.-Q. Zhao, M. Alhabeb, B. Anasori, E. C. Kumbur, H. N. Alshareef, M.-D. Ger, Y. Gogotsi, *Energy Environ. Sci.* **2016**, 9, 2847–2854.
- [47] Q. Jiang, C. Wu, Z. Wang, A. C. Wang, J. H. He, Z. L. Wang, H. N. Alshareef, *Nano Energy* **2018**, 45, 266–272.
- [48] C. Couly, M. Alhabeb, K. L. Van Aken, N. Kurra, L. Gomes, A. M. Navarro-Suárez, B. Anasori, H. N. Alshareef, Y. Gogotsi, *Adv. Electron. Mater.* **2018**, 4, 1700339.
- [49] H. Li, Y. Hou, F. Wang, M. R. Lohe, X. Zhuang, L. Niu, X. Feng, *Adv. Energy Mater.* **2017**, 7, 1601847.
- [50] N. Wang, J. Liu, Y. Zhao, M. Hu, R. Qin, G. Shan, *ChemNanoMat* **2019**, 5, 658–665.
- [51] N. Kurra, B. Ahmed, Y. Gogotsi, H. N. Alshareef, *Adv. Energy Mater.* **2016**, 6, 1601372.

Manuscript received: April 25, 2021

Accepted manuscript online: May 6, 2021